Leveraging Process Fundamentals to Improve Semiconductor Thickness Control and Uniformity in Inkjet-Printed Schottky Diodes

Jonathan D. Nguyen, Satish Kumar, C. Daniel Frisbie[*]*, Lorraine F. Francis*[*]

Department of Chemical Engineering and Materials Science, University of Minnesota, 421 Washington Avenue SE, Minneapolis, MN 55455, United States of America

*E-mail: lfrancis@umn.edu; frisbie@umn.edu

Keywords: uniformity, planarization, self-aligned, organic Schottky diode, printed electronics, drying

Abstract

Liquid-applied coating and printing methods are attractive options for large-area, low-cost production of flexible electronics. However, controlling the deposited functional layer thickness and uniformity, particularly at submicron thicknesses, is challenging. This study focuses on thickness uniformity and control in Schottky diodes made by Self-Aligned Capillarity-Assisted Lithography for Electronics (SCALE). SCALE combines UV imprinting to structure a substrate surface and inkjet printing of functional inks to make flexible electronic devices. In the diode described here, the key functional layer is the poly(3-hexylthiophene-2,5-diyl) (P3HT) semiconductor, which is deposited from a 1,2-dichlorobenzene solution. Thin, uniform P3HT layers with no shorts are required for optimal diode performance. Thickness nonuniformities in the P3HT layer, including the coffee-ring effect and lack of planarization over adjacent electrode channels, occurred during drying. These nonuniformities were most severe for drying at elevated temperatures (≥50°C). By drying P3HT layers at 23°C, the film uniformity and planarization improved significantly, and the device yield was nearly 8x higher. P3HT layers less than 300 nm thick are demonstrated. The improvements in uniformity and planarization are discussed in terms of the competition between solvent evaporation and P3HT diffusion. Self-aligned, printed Schottky diodes demonstrated up to 4.0×10^4 rectification ratio at ±1 V, minimal hysteresis, and ~0.3 V turn-on voltage.

1. Introduction

In recent decades, technological advances have expanded the electronics application space to include novel flexible and wearable electronic devices such as sensors[1], RFID tags[2], and smart packaging labels.[3] The prospect of fully integrating electronic systems into everyday items has

garnered considerable attention. New manufacturing methods that reliably produce low-cost, flexible electronics at high-throughput are needed to meet this demand.[4]

Liquid-applied printing processes are particularly promising due to their roll-to-roll (R2R) compatibility, low costs, and potential for large-area electronics applications such as displays and spatially distributed sensors. Several traditional printing techniques, including inkjet, gravure,[5,6] and screen[7] printing have been utilized. However, achieving layer-on-layer registration in these R2R processes is a challenge due to difficulties with alignment to plastic web.[4]

Inkjet printing is a promising manufacturing method that provides an additive, digital, no-contact route to high-throughput fabrication of solution-processed electronics.[8,9] Because inkjet printing is additive, the amount of waste generated is substantially reduced, which becomes increasingly crucial for R2R scale-up to minimize costs. Despite its strengths, inkjet printing still has challenges with resolution and achieving a high aspect ratio (thickness/width) due to ink spreading on the substrate. Typical inkjet printers achieve lateral resolutions on the order of tens of microns.[8,10] Resolution directly impacts device performance and device density. To improve the resolution limitation and enable layer-on-layer registration, our group developed a process termed SCALE (Self-aligned Capillarity-Assisted Lithography for Electronics). SCALE has been used to fabricate functional resistors,[11] capacitors,[12] diodes,[13] conductive wires,[14,15] and transistors.[16,17]

Figure 1 shows an overview of the imprinting stage of the SCALE process. SCALE combines ultraviolet (UV) microimprinting with inkjet printing to provide an R2R-compatible process for producing electronic devices on flexible substrates. In the UV microimprinting step, an elastomeric stamp is cast from a silicon wafer template patterned using photolithography (Fig. 1a). The stamp is then pressed onto a UV-curable resin coating on a plastic substrate (e.g., polyethylene terephthalate, polyimide) and UV cured (Fig. 1b,c). After stamp removal, an intricate network of

recessed reservoirs, capillary channels, and device structures with micron-level resolution remain on the substrate (Fig. 1d). UV microimprinted webs are produced continuously in an R2R process.[14]

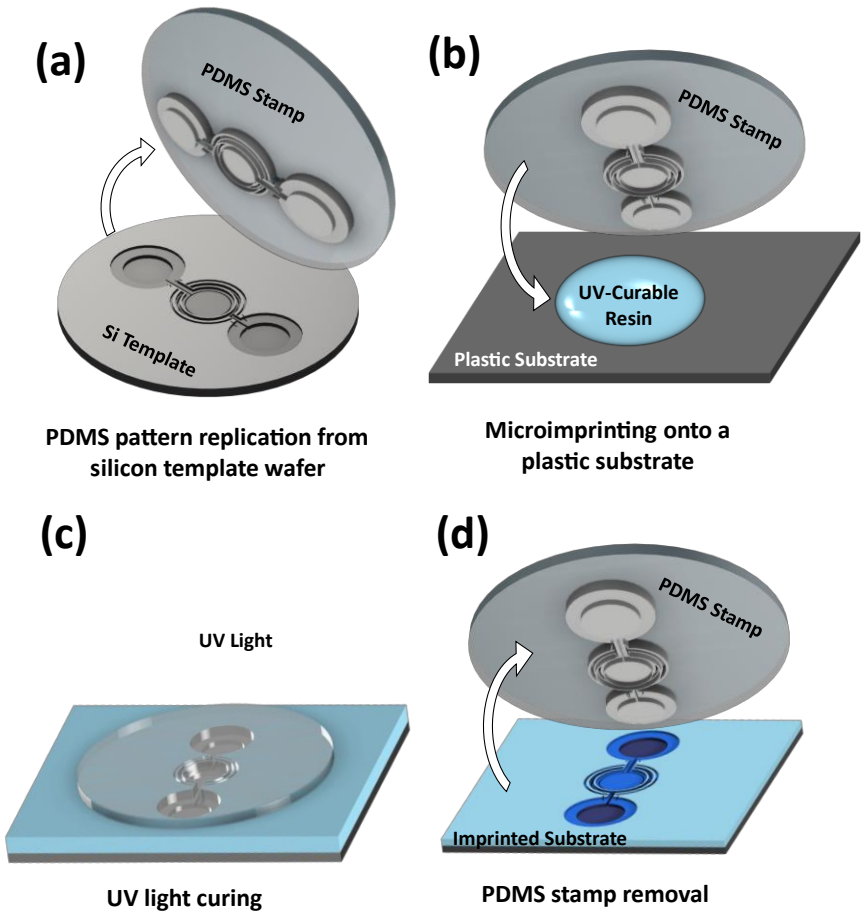

Figure 1. Schematic overview of each step in the SCALE UV imprinting process, beginning with (a) PDMS stamp casting from a photolithography patterned silicon template wafer, (b) microimprinting onto a plastic substrate using a UV-curable resin, (c) UV light exposure to cure the resin, and (d) removal of the PDMS stamp, leaving behind the patterned imprinted substrate into which inks can be deposited via inkjet printing. Note that only one device, not drawn to scale, is shown as an illustration.

The next stage of SCALE is the addition of functional inks to the imprinted substrate by inkjet printing. The imprinted web can be transferred to another R2R line for inkjet delivery to the reservoirs, capillary flow, and annealing. The SCALE process directly addresses both the resolution and the layer-on-layer registration problems of traditional inkjet printing methods. Because the deposited ink is confined within the imprinted pattern, the defining resolution for the overall process is dictated by the microimprinting step rather than the inkjet printing step. Thus, SCALE enables submicron resolution while retaining the additive nature and low cost of inkjet printing. To fabricate multilayer devices, such as the diodes in this study, functional inks are sequentially deposited into the reservoirs. The inks self-align with each deposition to coat imprinted features, eliminating the need for layer-on-layer alignment in complex device structures.

SCALE relies on precise control of flow and solidification of inks.[18] Most often in devices, a uniform thickness is ideal; therefore, nonuniformities associated with drying are a challenge. The coffee-ring effect, first extensively studied by Deegan et al.[19], is a nonuniform, ring-like deposit that stems from an advective flux of dispersed particles to the edges of drying droplets. The outward advective flux is caused by pinned contact lines and enhanced local evaporation at the droplet edge due to an increased probability of solvent molecules escaping into the vapor phase by random diffusion.[20] This effect is further enhanced due to a shorter thermal conduction length at the droplet edge, resulting in faster local heating and evaporation. In colloidal systems, this effect is well-studied,[20–26] and several approaches to mitigate coffee-rings have been demonstrated, including Marangoni flows,[27–29] anisotropic particles,[30] and adjusting pH.[31] However, for systems containing dissolved polymer, which is common for organic electronics, the effect is less studied and involves additional factors like polymer molecular weight, radius of gyration, and chain-chain

interactions.[32–35] Because inkjet printing is used in SCALE to deposit solutions of various materials, understanding of the coffee-ring effect and routes to mitigate it is paramount.

Careful control over the film thickness, uniformity, and morphology of each layer within a device is critical to the overall electronic performance. In Schottky diodes, a semiconductor layer is sandwiched between conductors to form two interfaces.[36] One is typically a metal-semiconductor Schottky junction that rectifies current due to a Schottky barrier arising from differences in the metal work function and semiconductor band edge. The other interface is an ohmic junction that facilitates connections between the diode and external circuitry. Schottky diodes exhibiting layers ~50 nm thick have been demonstrated using processes like spin-coating and vapor deposition.[37,38] A thin semiconductor layer is optimal to reduce the diode series resistance, which contributes to diode non-ideality and limits the operating frequency.[39,40] However, achieving sub-100 nm thicknesses using printing methods is a challenge. Typical inkjet printing processes achieve minimum layer thicknesses on the order of 0.5 – 3 μm.[41] The challenge lies in preventing short-circuits in printed diodes with increasingly thin semiconductor layers, which limits the minimum printed layer thickness that can be reliably achieved.[42] Building the active diode structure in a SCALE reservoir, for example, requires multiple depositions of ink, each of which pins to the corner of the reservoir that keeps the ink contained. After drying, local thinning at this corner leads to a possibility of the bottom contact shorting with the top contact (Fig. 2a).

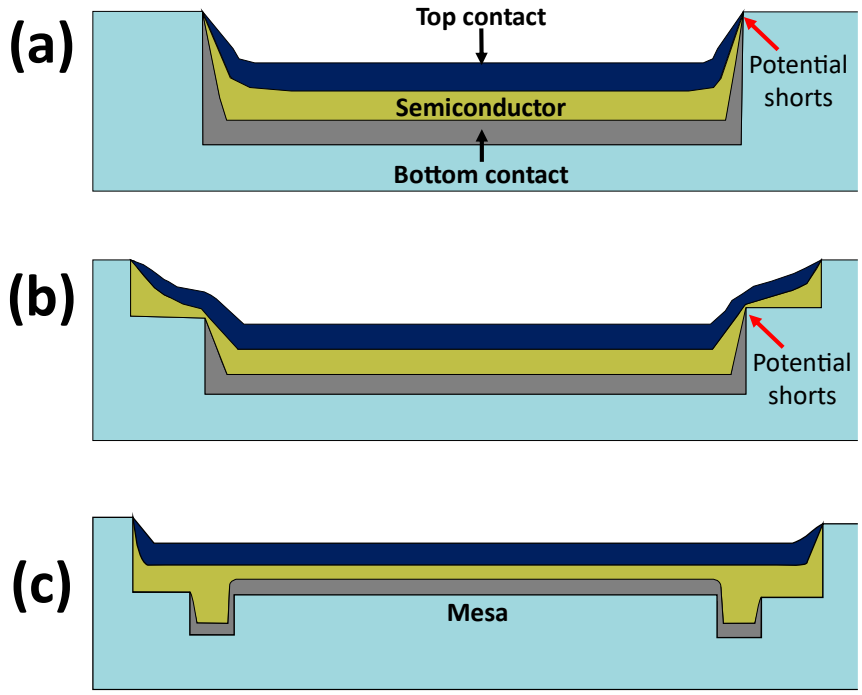

Figure 2. Schematic cross-sections of a reservoir in various diode geometries to illustrate challenges in fabricating SCALE multilayer devices. Each is a three-layer stack constructed by sequential deposition and drying of three inks within a circular recessed area on an imprinted substrate. The geometries consist of (a) a single-level reservoir, (b) a two-level reservoir, and (c) a mesa. See text for more description.

Cao et al.[13] fabricated SCALE Schottky diodes using a two-level reservoir device structure to avoid this shorting problem. The first electrode layer is confined in the lower-level reservoir (Fig. 2b), eliminating the three-material pinning point in the single reservoir device. Printed diodes with a $10^{3.5}$ on/off current ratio were fabricated. A SCALE diode was connected in series with a commercial capacitor to form an AC power rectifier circuit that rectified a 1 V AC signal of up to 1 kHz frequency.[13] However, this structure is still limited by susceptibility to short-circuit failure at the 90° corner between the two levels, particularly with thin semiconductor layers. The smallest semiconductor thickness found to maintain appreciable (90%) device yields in this past work was

1 μm. At a thickness of 500 nm, the yield dropped to 22%.[13] Thus, a new geometry is necessary to circumvent this issue and enable thinner semiconductor layers in SCALE diodes.

The current study reports a new Schottky diode based on a mesa geometry (Fig. 2c). This "mesa diode" is designed to reduce device failure via short-circuits by confining the bottom contact to the mesa and surrounding channels. By combining a mesa geometry with controlled drying conditions, semiconductor layers with 300 nm thicknesses were achieved. The films also have relatively flat surfaces over a nonuniform substrate topography, demonstrating planarization across an active region footprint of 0.16 mm^2. The effects of drying temperature on the uniformity of a deposited film from a pinned droplet on the mesa are explained using a Péclet number, which describes the relative effects of evaporation-induced advection and diffusion during drying. This framework is extended into the case where deposition of a film occurs over topographical features, where planarization during drying again depends on the competition between diffusion and evaporation. With the optimized process, functional organic Schottky diodes with over 10^4 rectification ratios, low hysteresis, and improved yields were achieved. Overall, the results demonstrate how device design and ink drying conditions can be tuned to improve Schottky diodes for printed electronics on flexible plastic in an R2R-compatible, self-aligned, and additive manner.

2. Experimental Section

2.1 Silicon Wafer Template Fabrication

The template for the mesa diode design was fabricated on a silicon wafer using conventional cleanroom photolithography. This design consists of three reservoirs, two for contacts and a central reservoir for the mesa diode. On a 4-in diameter, 500 μm thick silicon wafer (WaferPro), two cycles of photolithography were completed to (1) pattern the reservoirs and capillary channels to a depth of 5 μm and (2) pattern a 4 μm high elevated enclosure layer to contain the deposited ink.

Further details and parameters used during the photolithographic fabrication process are provided in the supporting information section S1. The silicon wafer template pattern was transferred to a flexible polydimethylsiloxane (PDMS; Dow Sylgard 184) stamp for use in UV microimprinting using a similar protocol described in prior work.[15,16]

2.2 UV Microimprinting onto Flexible Substrates

PDMS stamps were used to imprint the device design onto flexible polyimide substrates. Polyimide (Kapton HN, American Durafilm) sheets were cut to approximately 5×5 in^2, pre-cleaned using isopropanol, and dried in air. The Kapton sheets were treated in an O_2 plasma cleaner (Harrick Plasma PDC-32G) at 0.8 torr, 18 W RF power for 3 min to improve adhesion in the following step. After depositing UV-curable resin (NOA73, Norland Optical Adhesives) onto the treated Kapton sheet, the PDMS stamp was pressed onto the resin. The entire stamp-imprint structure was then placed in a UV curing chamber (Honle LED Cube 100) and exposed to 3 cycles of ~30 mW cm^{-2} UV light for 90 s each cycle. Afterward, the PDMS stamp was peeled off while the patterned resin remained adhered to the Kapton backing.

2.3 Device Fabrication

Organic Schottky diodes were fabricated using inkjet printing on the imprinted substrate. The sequence of printing operations is described in more detail in section 3.1. All inks were deposited using a custom drop-on-demand inkjet printer comprised of a controller (MicroFab JetDrive III) paired with an 80 μm diameter nozzle (MicroFab Technologies, Inc.). The controller sends tunable, unipolar waveforms to a piezoelectric in the nozzle, causing subsequent ejection of ink droplets onto the imprinted substrates. For all inks, the waveform frequency was set to 1000 Hz with a rise, dwell, and fall time of 3, 20, and 3 μs, respectively. The dwell voltage was set to 60-70 V. All inks

were filtered with 0.22 μm pore size polytetrafluoroethylene or water-wettable polytetrafluoroethylene filters prior to printing.

To form the bottom and top contacts, particle-free reactive silver (Ag) ink (ElectronInks EI-011) was first deposited onto the mesa, followed by a hotplate bake at 140°C for 1 min. Then, two layers of Ag ink were printed into the bottom and top contact reservoirs, with a hotplate bake at 140°C for 1 min after each layer. The double-printed Ag into the contact reservoirs ensures the formation of a contiguous Ag connection. The Ag was then photonically sintered using an intense pulsed light (IPL; Sinteron 2010, Xenon Corp) source that uses a xenon lamp to deliver broadband spectrum (190-1100 nm) energy. The Ag was exposed to a single pulse of 2.5 kV amplitude and 4905 μs width for an overall energy dosage of 10 J/cm^2. The lamp-to-sample distance was 4 cm.

Poly(3-hexylthiophene-2,5-diyl) (P3HT) was printed to form the active layer of the device. The P3HT (regioregular, molecular weight = 50-70K, Rieke Metals) was added to 1,2-dichlorobenzene (oDCB; Acros Organics) to achieve a concentration of 30 mg/ml and dissolved by heating at 65°C for 2 h with constant stirring at 800 rpm on a hotplate. After cooling, the ink was printed into the central device reservoir and then dried at 23°C (ambient conditions). A secondary bake was completed at 140°C for 30 min under inert N_2, which is reported to induce the formation of crystalline fibrils that improve charge transport.[43,44]

Finally, a layer of conductive poly(3,4-ethylenedioxythiophene):polystyrene sulfonate (PEDOT:PSS) was printed to connect the device stack to the top Ag contact and complete the device. Commercial PEDOT:PSS ink (Heraeus; Clevios PH1000) was prepared with 6 wt% ethylene glycol (VWR Chemicals) and 3 wt% Triton X-100 (Sigma-Aldrich) as additives to improve both the ink conductivity and wetting behavior.[45–48] The ink was dried at 23°C (ambient conditions) in air, followed by 10 min at 140°C under inert N_2 to improve conductivity.[49] In a R2R

process, an inline IR heater could be used to replace the hotplates to rapidly heat the samples, reducing the drying and annealing times substantially. This technique shows promise and has been demonstrated.[50,51]

2.4 Device Characterization

Device current-voltage (I-V) characteristics were measured in ambient air using a two-point probe setup with a source meter (Keithley 2612B). A bias was applied to the diode top PEDOT:PSS contact and swept from -1 V to 1 V at a rate of 0.2 V/s. The bottom contact remained grounded. Diode cross-sections were imaged in secondary electron mode using scanning electron microscopy (SEM; Hitachi SU-8230). Cross-sections were prepared by embedding devices in epoxy resin (Poly/Bed 812, Ted Pella Inc) for 24 h at 60 °C. Rough cross-sectioning was performed using a razor blade, after which fine cross-sectioning was completed using a microtome (Leica UC7). Surface micrographs were taken with a digital optical microscope (Hirox KH-7700).

2.5 P3HT Mesa Uniformity and Planarization Studies

To study the uniformity of P3HT films after drying, P3HT/oDCB solution was inkjet printed on top of the central mesa of the imprinted substrate (see section 3.1 for details of the geometry) to create a droplet pinned at the mesa edges. Most experiments were carried out on pinned droplets prepared by jetting 80 drops, which corresponds to a volume of ~21 nL, based on a 40 μm jetted drop radius (half the nozzle diameter). The deposits were dried on a hotplate under varying temperatures ranging from 23°C to 90°C for 1 min. Two-dimensional (2D) and three-dimensional (3D) topography profiles were characterized using stylus profilometry (KLA Tencor P-7) and a digital microscope (Keyence VHX5000), respectively. The effect of deposit volume was studied by controlling the number of jetted drops, resulting in volume ranging from 11 nL to 32 nL.

To study the effects of drying temperature on the extent of planarization, 21 nL of P3HT were deposited into the central reservoir to cover the mesa and surrounding channels. Again, this study was carried out directly on the imprinted substrate. The deposits were dried at temperatures ranging from 23°C to 120°C for 1 min. Cross-sections were cut and imaged using a focused ion beam/scanning electron microscope (FIB/SEM; FEI Helios Nanolab G4) to quantify the extent of planarization.

3. Results and Discussion

3.1 Mesa Design Overview

Figure 3 is an overview of the fabrication of organic Schottky diodes using the SCALE mesa design (for detailed design dimensions and optical micrographs of individual layers, see supporting information Figs. S2 and S3). The device structure is divided into three regions: top contact, device region, and bottom contact (Fig. 3a (top)). The accompanying cross-section across the device region shows the key structural features of the design, including the mesa (diameter = 450 μm), the channels (depth, width ~ 5 μm) surrounding the mesa circumference, the inner ring region (depth = 4 μm), and the outer ring region (depth = 4 μm) (Fig. 3a (bottom)). First, a particle-free reactive Ag ink is printed into both top/bottom contact reservoirs (diameter = 500 μm, depth = 5 μm) and on top of the central mesa. After drying and annealing, a layer of Ag is deposited, as shown in Figure 3b. The Ag deposited atop the mesa remains confined due to contact line pinning at the edges of the mesa circumference. The bottom contact reservoir supplies Ag ink to the capillary channels surrounding the mesa, depositing a layer of Ag over all of the interior channel surfaces. This coating establishes an electrical connection to the Ag on top of the mesa with ~40 Ω resistance, as verified by two-probe measurements. The top contact reservoir supplies Ag ink to

the lower level of the two-level capillary channels in the outer ring around the central mesa. This outer ring Ag structure is used to make the top contact (see Fig. 3b).

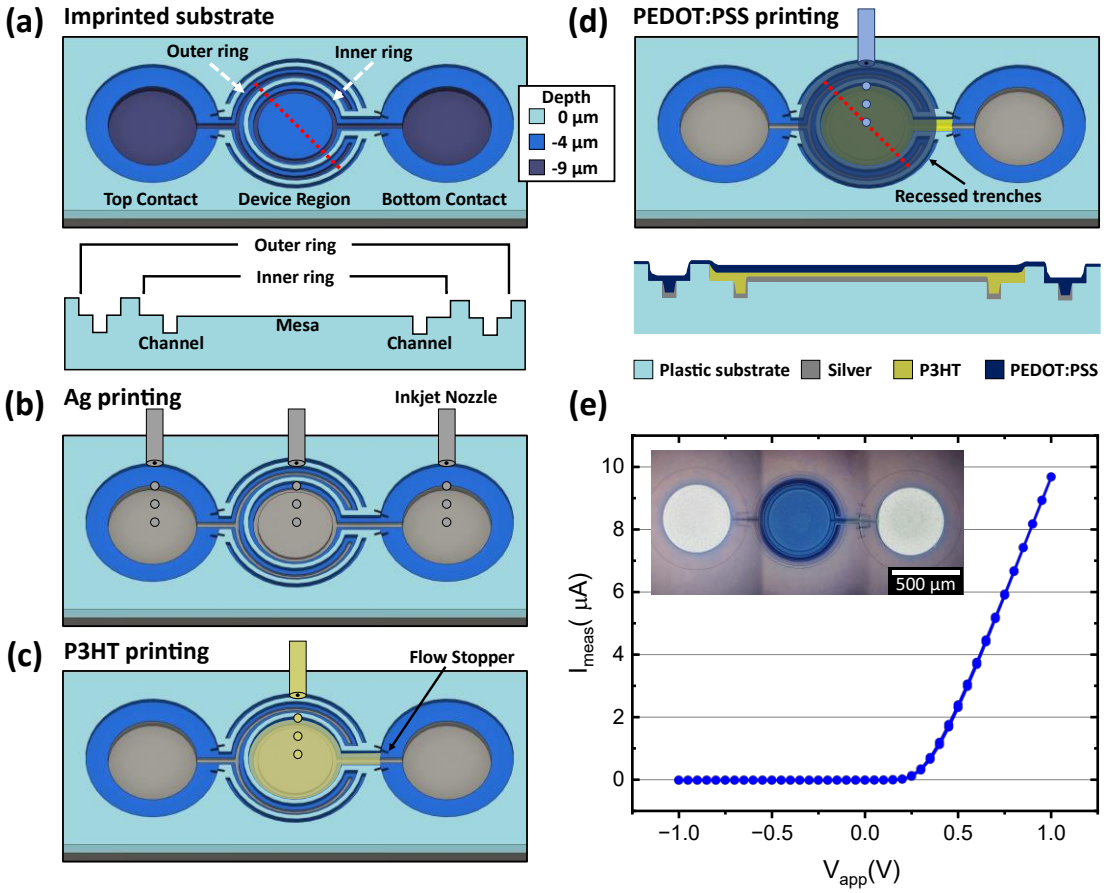

Figure 3. Overview of the mesa diode design fabrication steps. (a) (Top) Isometric view of the imprinted substrate and (Bottom) corresponding cross-sectional schematic along the dashed line detailing key structural features of the design. (b) Ag printing to form the bottom contact and part of the top contact. (c) P3HT printing over the mesa and within the inner ring. (d) (Top) PEDOT:PSS printing to complete the top contact and (Bottom) schematic cross-section of the completed diode. (e) Typical current-voltage curve obtained from a mesa diode demonstrating rectification. The inset shows a composite optical micrograph of the completed diode.

Next, P3HT ink is deposited into the inner ring region to cover the Ag on top of the mesa and fill in the inner ring channels upon drying (Fig. 3c). The P3HT flows towards the bottom contact reservoir until it pins at two rectangular depressions, termed flow stoppers.[13,16] These flow stoppers are recessed structures that prevent the P3HT ink from spreading onto the Ag within the bottom

contact reservoir. Lastly, a layer of PEDOT:PSS ink is deposited onto the entire central device region, contacting both the P3HT in the inner ring and the Ag in the outer ring channels (Fig. 3d (top)). The deposited PEDOT:PSS is contained by recessed trenches (depth = 4 μm) around the outer ring that pin the contact line at the 90° corners.

The central device region contains a mesa and surrounding channels encompassing the inner ring around the mesa. The cross-section of this region depicts the materials stack that forms the Schottky diode (Fig. 3d (bottom)). The P3HT, an organic p-type semiconductor, is sandwiched by Ag metal on the bottom and PEDOT:PSS on top. The Ag-P3HT interface forms the rectifying Schottky junction, while the P3HT-PEDOT:PSS interface forms the ohmic junction. Importantly, because the Ag is selectively deposited within the inner channels and atop the mesa, the Ag bottom contact beneath the P3HT is less susceptible to shorting with the PEDOT:PSS top contact compared with the previous design (see Fig. 2b). An optical micrograph and typical current-voltage curve of the completed diode are shown in Figure 3e, demonstrating diode operation and rectification of current.

The two distinctive features of the P3HT layer shown in Figure 3d (bottom) are: (i) uniform thickness across the mesa surface and (ii) a flat surface across the channels surrounding the mesa. To achieve this ideal structure, an in-depth understanding of the deposition and drying behavior of the P3HT solution is essential. Successful demonstration of both features is critical to achieving high-performance diodes with minimal short-circuits. While thickness uniformity and a flat or planarized surface are inherently intertwined, our studies focused first on each criterion independently, before applying both towards the mesa diode design.

3.2 P3HT Thickness Uniformity on the Mesa

Figure 4 shows the effect of drying temperature and deposited solution volume on the uniformity of P3HT films deposited directly on the imprinted mesa (without Ag or PEDOT:PSS; Fig. 3a (top)). While this step is not used in the diode construction, it was investigated to determine the role of coffee-ring behavior during drying. After depositing an initial volume of 21 nL of P3HT solution, the ink was dried at varying temperatures ranging from 23°C to 90°C. The entire mesa was covered with P3HT solution after deposition; the contact line was pinned on the sharp edge of the mesa during drying. Profilometry scans of the dried films show a stark transition in deposition profile between specimens dried at 23°C and those dried at higher temperatures (Fig. 4a). In the 23°C drying case, a mound-like deposit forms with material concentrated at the center of the mesa. In the 50°C drying case, a crater-like deposit forms with material concentrated around the mesa edge, as indicated by two distinct peaks. After drying at 70°C and 90°C, the accumulation at the edge sharpens while the thickness at the mesa center remains relatively unchanged. The 3D profile scans (Fig. 4b) confirm that this drying behavior occurs uniformly around the mesa circumference. At 90°C drying, the peak P3HT thickness lies along the circumference of the mesa, forming a ring-like buildup. At 23°C drying, the peak P3HT thickness lies at the center of the mesa, while the thickness steadily decreases outward radially.

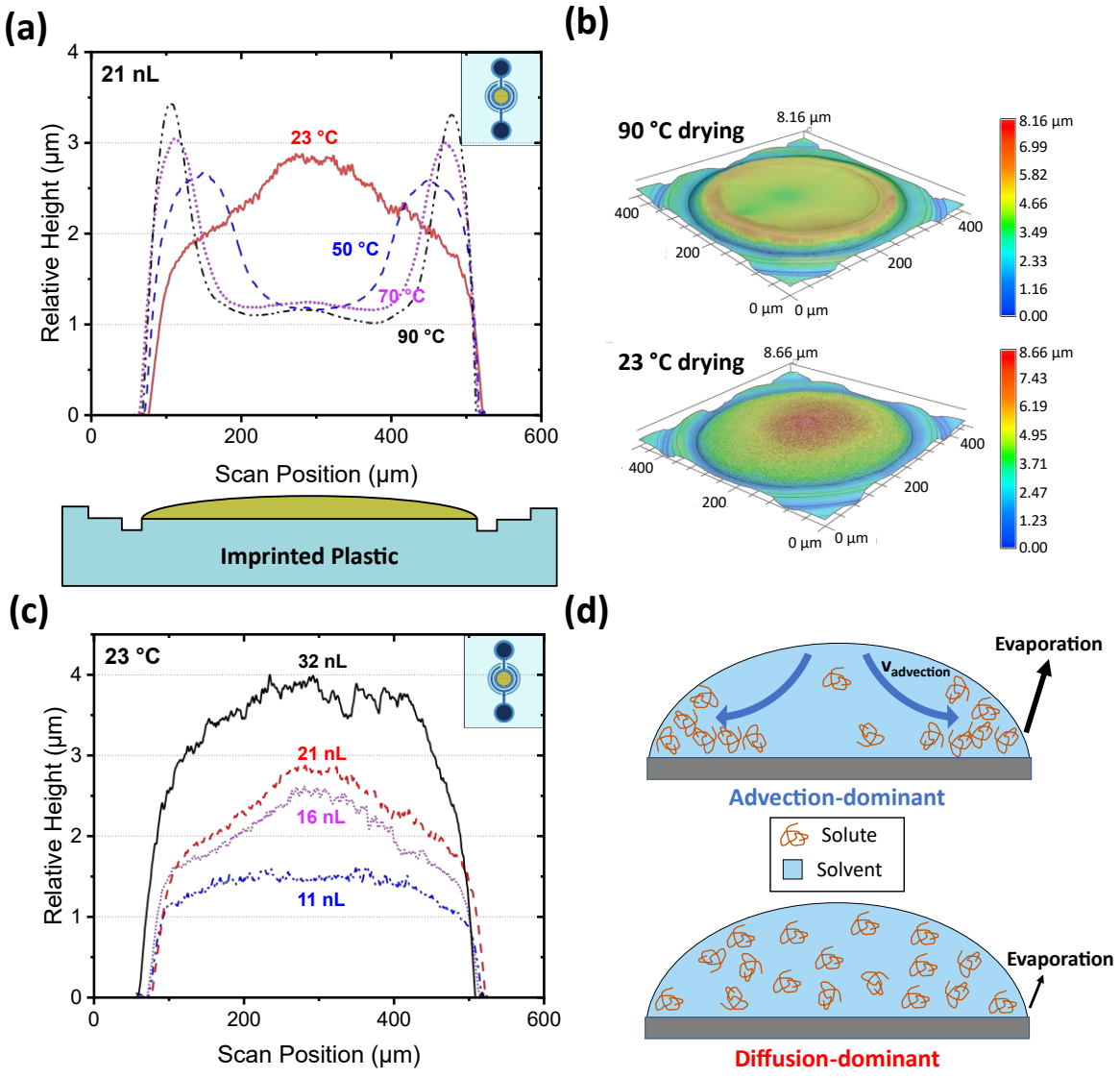

Figure 4. Effects of drying on the topography of deposited P3HT films. (a) Linear profilometry scans of 21 nL P3HT deposits atop the mesa after drying at varying temperatures. The bottom inset depicts the cross-section of P3HT on the mesa. The upper-right inset depicts the top-down view. (b) 3D profiles of P3HT films after drying at 90°C and 23°C. (c) Linear profilometry scans of P3HT deposits of varying volume dried on top of the mesa at 23°C. (d) Proposed transport mechanisms dominant under different drying conditions.

Figure 4c shows the profilometry scans of P3HT films prepared from ink deposits ranging in volume 11 nL to 32 nL, all dried at 23°C. Note that the sharp changes in height at the left and right

edges of the mesa do not reflect the absolute thickness due to convolution with the stylus geometry, (1 μm tip radius, 60° cone angle) but relative differences are meaningful. In the 16 and 21 nL cases, similar behavior as discussed previously is observed, with a mound-like deposition profile. Notably, in the smallest volume case of 11 nL, the mound-like deposition becomes less pronounced and the profile is flatter. As a metric for uniformity, we calculated the average thickness and standard deviation along the top surface of the P3HT films. To eliminate stylus geometry artifacts, we excluded 10% of the scan width from both the left and right mesa edges, using only the center 80% in the calculation. The results are summarized in Table 1. By reducing the volume of deposited solution, the film uniformity improved substantially. Comparing the results of the 21 nL deposit dried at 23°C and 90°C, the uniformity improved dramatically for drying at 23°C. These results suggest that more uniform P3HT films can be achieved through the reduction of both drying temperature and deposited volume, which is promising for achieving submicron films using printing techniques.

Table 1. Comparison of P3HT film uniformity with varying ink volume dried at 23°C and 90°C.

Volume [nL]	Drying Temperature [°C]	Average thickness [μm]	Standard deviation (% of average thickness) [μm]
32	23	3.52	0.37 (10.5%)
21	23	2.35	0.35 (14.9%)
21	90	1.46	0.66 (45.2%)
16	23	2.07	0.33 (15.9%)
11	23	1.41	0.12 (8.5%)

The results in Figure 4a show that the coffee-ring effect is present in the P3HT/oDCB system, and that one route to mitigate it is to reduce the drying temperature. As solvent evaporates at the

mesa edge, the pinned contact line requires an outward advective flow that carries P3HT to the mesa edge, resulting in a ring-like deposit. Interestingly, at lower drying temperatures this ring-like deposit is replaced by a mound-like deposit. At the lower temperatures, there appears to be an effective counteraction to the outward advective flow. One possibility discussed by Hu and Larson[27] is an inward thermal Marangoni flow generated by a surface tension gradient along the liquid-air interface. The surface tension gradient stems from a radial temperature gradient in the droplet caused by thinning of the droplet at the edge, leading to faster conductive heating from the substrate below the drop.

The effect of thermal Marangoni flows in polymer solutions was reported by Kim et al.[52] for a drying droplet of two systems: (i) PEDOT:PSS/water and (ii) poly(3-dodecylthiophene-2,5-diyl) (P3DDT)/anisole. For the PEDOT:PSS/water system, they observe that the deposit pattern is mound-like near room temperature, while with increasing drying temperatures the deposit transitions into an edge-concentrated, coffee-ring pattern. However, for the P3DDT/anisole system, they observed a ring-like deposit after evaporation over a range of temperature, even at room temperature. They suggest that a large surface tension temperature coefficient and high contact angle are responsible for producing an inward Marangoni flow in the PEDOT:PSS/water system. Whereas, in the P3DDT/anisole system, a small surface tension temperature coefficient and smaller contact angle lead to a dampened Marangoni flow. Small temperature coefficients indicate smaller changes in surface tension with temperature, while smaller contact angles minimize temperature gradients along a droplet surface. Both factors suppress Marangoni flows. The P3HT/oDCB system studied here has a small temperature coefficient of surface tension[53,54] (~0.12 mN/m·K), similar to P3DDT/anisole and a small contact angle (~10°) (see supporting information Fig. S4). When drying at 23°C, the temperature gradient across the surface is expected

to be minimal due to the small contact angle and lack of an external heat source. Thus, the effects of thermal Marangoni flows are expected to play a minor role in this case.

Another possibility is a temperature gradient along the free surface arising from evaporative cooling. Ristenpart et al.[55] demonstrated the effect of the ratio of the thermal conductivity of the substrate and liquid on the direction of Marangoni circulation. The thermal conductivity of 1,2-dichlorobenzene is reported as 0.12 W/m·K.[56] While the thermal conductivity of the NOA73 substrate is not known, the values for other UV-curable resins are reported to be ~0.20 W/m·K.[57,58] The resulting ratio of ~1.67 results in an outward Marangoni flow for contact angles less than ~25° according to Ristenpart et al.[55] Based on the measured contact angle and estimated thermal conductivity ratio, a radially outward thermal Marangoni flow would be expected. Yet, the results in Figure 4c show no coffee-ring effect at 23°C drying, indicating that thermal Marangoni flows have little discernible effect on the solute deposition.

Solutal Marangoni flows may also be a factor. Solute concentration gradients can give rise to surface tension gradients along the liquid free surface, thereby inducing solutal Marangoni flows that can affect the final deposition of solute. Measurements of surface tension (see supporting information Fig. S5) of P3HT/oDCB solutions were taken to examine the dependence of surface tension on solute concentration. The range of concentrations spanned from 0 to 100 mg/ml to encompass the 30 mg/ml concentration solutions used in this study. The results indicate that the change in surface tension with increasing solute concentration is small (<1 mN/m). Typical surface tension gradients reported for solutal Marangoni flows are on the order of 10 mN/m.[59–61] Hence, solutal Marangoni effects are not expected to play a significant role in the final solute deposition.

Lateral diffusion is another possibility for mitigation of the coffee-ring effect. As mentioned, reducing the temperature slows the evaporation rate, which in turn weakens the outward advective

flow of P3HT solute towards the pinned contact line. Concurrently, an extended evaporation time enables lateral diffusion of P3HT away from the contact line, where the concentration is elevated by enhanced evaporation (Fig. 4d). Generally, a Péclet number is used to compare the relative effects of random, microscopic events to that of averaged, macroscopic phenomena.[62] Here, a Péclet number can compare the relative effects of lateral diffusion to advection within a drying droplet[32,35]:

$$Pe = \frac{\text{Evaporation induced advection}}{\text{Diffusion}} = \frac{v(T)}{D(T)/l} \quad (1)$$

where v, D, l, and T represent advection velocity, solute diffusivity, characteristic length (mesa radius), and temperature, respectively. It should be noted that this comparison treats the dissolved polymer as individual separate chains in solution and does not account for possible aggregation during drying. The advection velocity is the lateral velocity of the solute toward the pinned edge of the drying solution droplet on the mesa. This velocity is equal to the rate of the solvent removal by evaporation at the pinned edge. Thus, the advection velocity is directly proportional to the rate of evaporation at the edge, as shown below:

$$Pe = \frac{v(T)}{D(T)/l} = \frac{\text{Evaporation}}{\text{Diffusion}} = \frac{cE_0(T)}{D(T)/l} \quad (2)$$

where E_0 is the evaporation rate in volume lost per unit time per unit surface area during the initial drying stage and c is a geometric constant that accounts for the enhanced evaporation at the pinned edge ($c > 1$).

To quantitatively compare values for Pe at different temperatures, both the evaporation rate and diffusivity must be estimated. The evaporation rate during the early stages of drying was approximated based on mass loss experiments performed with oDCB (see supporting information

Section S6 and Figs. S7-9 for details). The evaporation rates for 23°C and 90°C drying were found to be ~0.01 μm/s and ~0.14 μm/s, respectively. Therefore, it is expected that conditions with high drying temperatures lead to larger *Pe*, and accumulation at the edges is expected due to the dominant effects of advection. However, the temperature dependence of the diffusivity must also be considered.

Diffusivity values for P3HT were approximated using the Rouse-Zimm model and Stokes-Einstein relation[63,64] as 1.05×10^{-7} cm^2/s and 2.69×10^{-7} cm^2/s for 23°C and 90°C, respectively (see supporting information Section S6). Notably, the relative sensitivity to temperature of evaporation is about an order of magnitude larger than that of diffusivity. Thus, increasing the drying temperature significantly amplifies evaporation while having a lesser effect on solute diffusion. As shown in Figure 4a, when drying at ≥ 50°C, the coffee-ring buildup was observed, indicating that faster evaporation drove a stronger advective flow to the pinned contact line. Conversely, in the 23°C case, evaporation—and thus advection—was suppressed, enabling diffusion to prevent accumulation at the contact line. This diffusion promotes a more uniform solute distribution within the droplet, resulting in the mound-like deposition upon drying that resembles the droplet shape.

Using these estimates for evaporation rate and diffusivity, values of *Pe* were calculated to be $0.23c$ for 23°C and $1.15c$ for 90°C (for detailed calculations, see supporting information section S6). Drying at 23°C resulted in a smaller *Pe* value, and thus, mitigation of the coffee-ring effect. Eales et al.[35] present numerical results that confirm that lower *Pe* values can eliminate the coffee-ring effect. Furthermore, these experimental results corroborate the model proposed by Okuzono et al.[65] to predict the final shape of drying polymer films in the limit of slow evaporation. They report that in the absence of diffusion, a “crater shape” forms in their model predictions, like our

90°C drying case. However, after incorporating the effects of diffusion into their model, a "mound shape" deposit arises, like our case of 23°C drying.

As shown in Figure 4c, reducing the droplet volume led to improvements in the uniformity of the deposited P3HT layer dried at 23°C. One possible reason for this effect may be due to a change in contact angle. When an initial droplet is deposited, it wets the mesa with an equilibrium contact angle. As increasing volume is added, the droplet area expands, spreading across the mesa while maintaining its equilibrium contact angle. However, once enough volume is deposited such that the droplet covers the entire mesa surface, it becomes pinned at the sharp mesa edges. From here, any additional volume added increases the contact angle to a nonequilibrium state, which results in a less uniform droplet height and subsequent film upon drying. For all the volumes used in Table 1, the droplet covers the entire mesa. Thus, there is an inverse trend where decreasing volume improves uniformity.

3.3 Planarization of P3HT over Topography

Depositing materials layer-by-layer over uneven topography is often necessary for the fabrication of electronic devices using solution processing methods. To investigate whether the improved uniformity via drying temperature reduction found for a pinned drop on the mesa extends to the mesa and channel geometry, 21 nL of P3HT ink was deposited over the entire inner ring region of the bare imprinted substrate (no Ag or PEDOT:PSS). Figure 5 shows cross-sections of the P3HT films dried at various temperatures. Here, the P3HT not only deposits on top of the mesa, but also spans across the channels. An optical micrograph of the deposited film after 23°C drying (Fig. 5a (left)) with corresponding schematic cross-section is shown. To quantify planarization, we adapt a metric from Bornside et al.[66]:

$$\text{Degree of Planarization (DoP)} = \left(1 - \frac{\Delta_{coating}}{\Delta_{substrate}}\right) \times 100\% \quad (3)$$

where $\Delta_{coating}$ is the height change of the coating due to the channel and $\Delta_{substrate}$ is the height change of the substrate (i.e., the channel depth). Figure 5a (right) illustrates a physical depiction of these quantities. A DoP of 100% indicates perfect planarization, whereas 0% represents a conformal coating with no planarization.

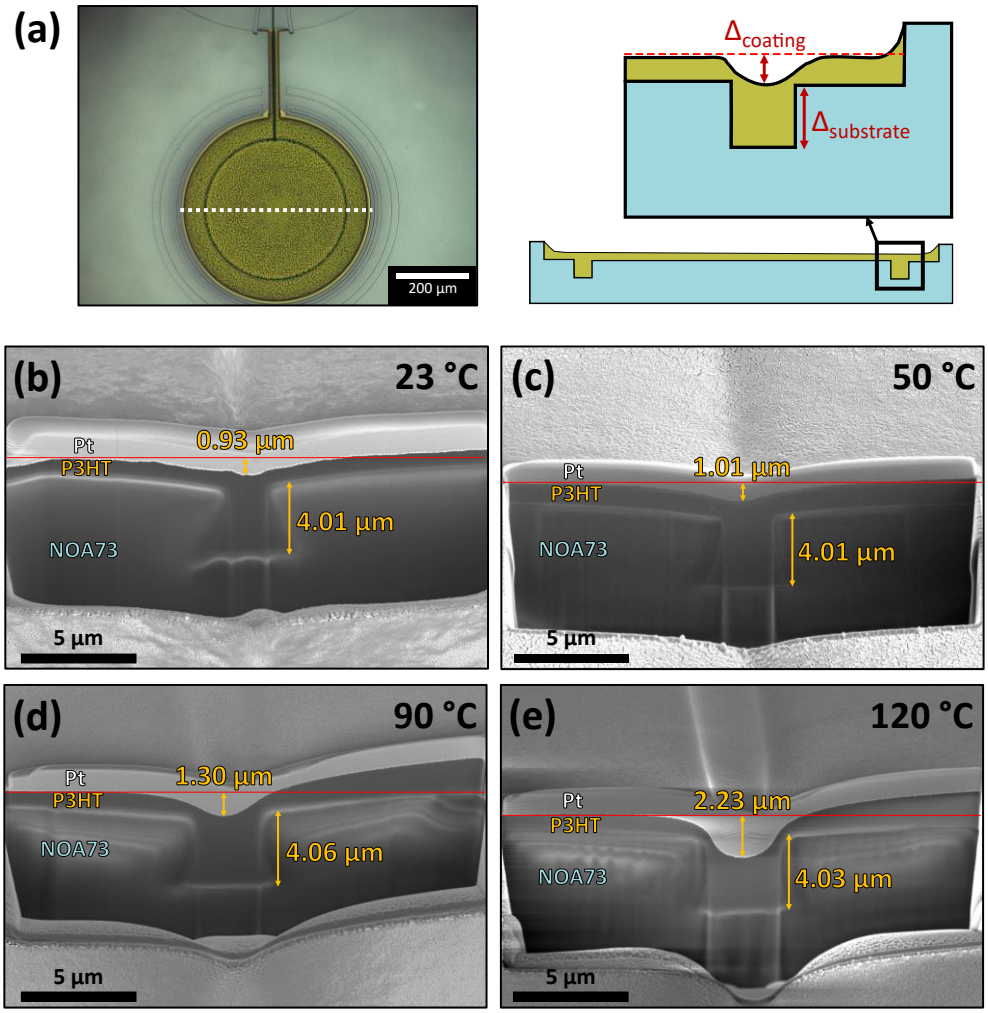

Figure 5. The effects of drying temperature on planarization of recessed channels. (a) (Left) An optical micrograph of the as-deposited P3HT and (Right) corresponding schematic cross-section. The black box denotes the region of interest. The magnified channel schematic depicts the quantities used to define degree of planarization. Scanning electron micrographs of the cross-sections at the channel are shown after drying at (b) 23°C (c) 50°C (d) 90°C (e) and 120°C. The thin, red line denotes the top surface of the deposited P3HT film. A platinum protection layer was deposited prior to cross-sectioning to improve image contrast. Note that channel distortions are an artifact of ion beam damage to the sensitive polymeric materials.

Cross-sectional scanning electron micrographs of the dried P3HT films taken at the mesa channel demonstrate the effect of drying temperature on planarization. After 23°C drying, the P3HT fully fills in the channel and forms a relatively flat layer across the channel that has a DoP of 77% (Fig. 5b). At 50°C, the P3HT again fully fills in the channel, although a slight dip begins to arise, bringing the DoP down to 75% (Fig. 5c). As the drying temperature ramps up to 90°C, the dip over the channel becomes increasingly dramatic, dropping the DoP to 68% (Fig. 5d). Lastly, at the extreme of 120°C drying, the dip over the channel becomes drastic, extending beyond the channel opening and into the channel itself, resulting in only 45% planarization (Fig. 5e). These data indicate that higher drying temperatures are harmful for planarization, manifesting as dips in the P3HT over the channel. These dips can become problematic, as they give rise to potential points for short-circuits in a device if the underlying Ag within the channels becomes exposed due to incomplete channel filling. In the ideal case, a thin layer of P3HT extends across the entirety of the mesa with channels fully filled such that shorting is prevented.

Figure 6 shows a schematic depicting the proposed progression of planarization during drying of a P3HT solution coated over an isolated channel, far from any edges or contact line pinning points. Initially, solute is uniformly distributed throughout the solution (Fig. 6a). As drying begins, solvent evaporates evenly across the descending free surface. As evaporation proceeds, a lateral concentration gradient develops as the free surface approaches the channel due to the greater volume of solution in the channel region. The average solute concentration within the channel is lower than the average solute concentration outside of the channel, and the resultant lateral concentration gradient causes polymer solute to diffuse laterally from the high concentration region to the low concentration region within the channel (Fig. 6b and 6c). The lateral diffusion

continues, resulting in a fully filled, planarized channel upon complete drying (Fig. 6d). However, if the evaporation rate is fast enough, the time available for lateral diffusion is limited and less planarization is observed.

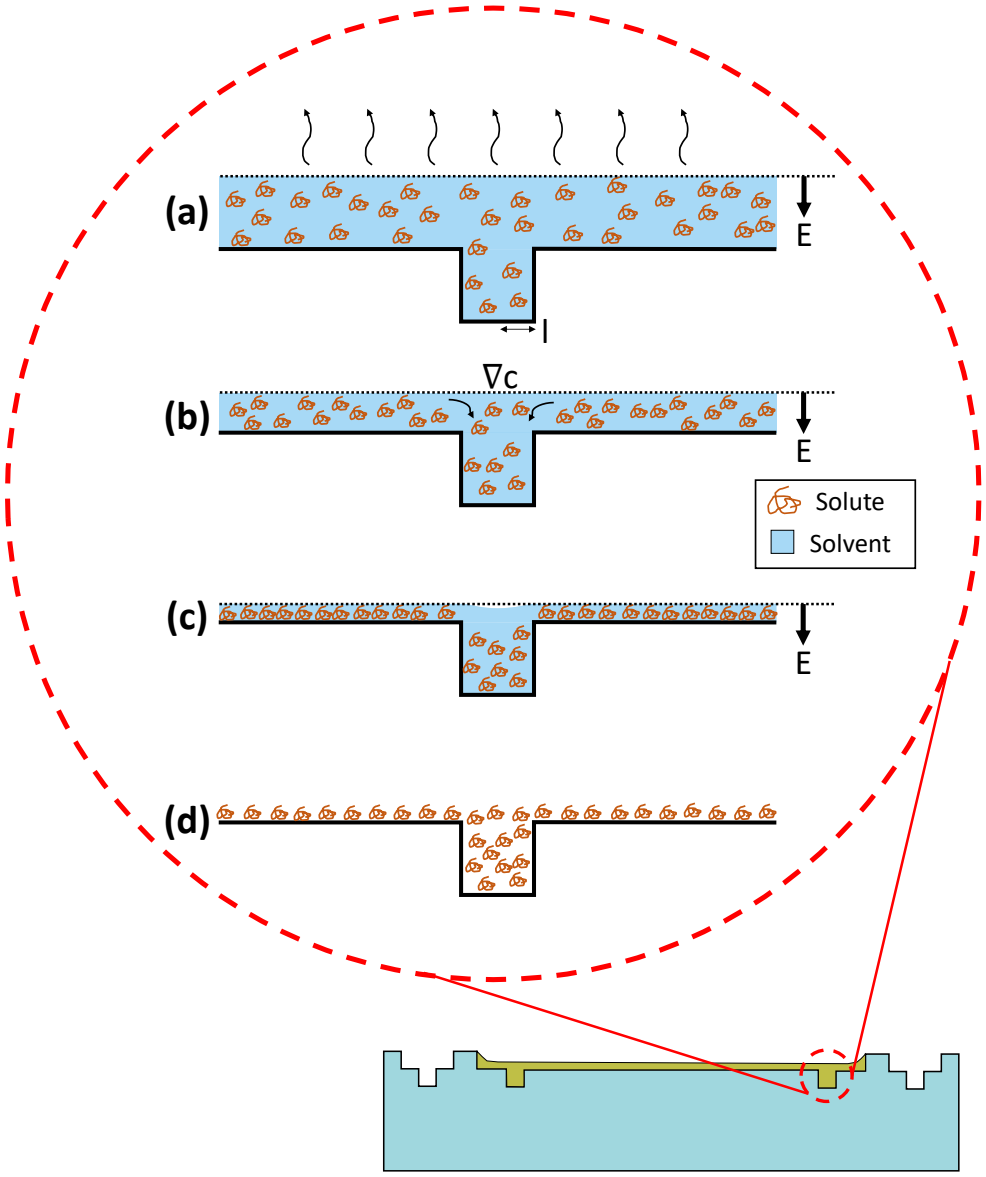

Figure 6. Schematic of the planarization process over an isolated channel of width 2l. (a) Initially, solute is uniformly concentrated throughout the solvent. Solvent evaporates at a rate E, given as the velocity of the descending free surface. (b) As evaporation proceeds, a concentration gradient ∇c causes solute diffusion into the channel. (c) Longer drying times enable increased channel filling via diffusion. (d) Upon complete drying, the channel is fully filled, leaving behind a planarized film.

Another factor to consider is that a top-down concentration gradient may also develop during drying (not shown in Fig. 6) with the free surface having a higher P3HT concentration; this effect could delay the onset of a lateral concentration gradient. Prior literature describes this type of planarization for spin-coating over substrates with recessed channels.[66–68] Bornside et al.[66] predicted polymer concentration in a polymer-solvent coating during drying after the spin-off stage. They found that a top-down concentration gradient develops first with the free surface having the same concentration independent of the position of the channel. Then, later in the drying process a lateral concentration gradient develops around the recessed channel, as mentioned above, and drives diffusion of solute into the channel. They also demonstrated that the degree of planarization decreased with increasing spin speed, as higher spin speed resulted in faster evaporation. After the spin-off stage, the coating thickness decreases due to evaporation alone. Hence, the loss in planarization with increasing spin speed is connected to faster thinning of the coating by evaporation and less time for lateral diffusion to fill in the channel. The results shown in Figure 5 are analogous; faster evaporation at higher temperatures results in less time for diffusion and less planarized channels.

Thus, planarization also involves a competition between diffusion and an evaporation-dependent velocity, like advection velocity for the case of solution drying on a mesa. Here, the velocity of interest is the velocity of the descending free surface, E. Therefore, the Péclet number definition (Eqn. 2) used for a droplet drying on top of a mesa can also be used to explain the temperature dependence of planarization. In this case, the characteristic length is chosen as half of the channel width, 2.5 μm, and the geometric constant $c = 1$ for a flat evaporation surface. In an evaporation dominated (high Pe) system, rapid evaporation proceeds, and solute has little time for lateral diffusion, resulting in deposition of a conformal layer. In the diffusion dominated (low Pe) regime,

slower evaporation allows for increased solute diffusion time, allowing for the deposition of a planarized layer.

Using the diffusivities and evaporation rates discussed previously in section 3.2, calculated values for *Pe* are 2.6×10^{-3} for 23°C and 1.3×10^{-2} for 90°C (for detailed calculations, see supporting information section S10). These values are much lower than the previous *Pe* values found for the mesa uniformity study because $c = 1$ and the chosen characteristic length scale for diffusion is smaller, i.e., half of the channel width. In practice, to fill the channel, solute diffuses from a region that extends beyond the channel width. The increase in drying temperature leads to a five-fold increase in *Pe*, favoring evaporation over lateral diffusion. For the mesa diode design, a smaller *Pe* is desirable to maximize channel filling and eliminate potential sites for short-circuit failure. It is important to note that increasing solute lateral diffusion time is only one parameter that controls planarization. Additionally, there is a component of vertical diffusion, where the descending free surface can lead to a vertical concentration gradient. Here, the characteristic length is the initial coating thickness, which results in a larger *Pe* as the coating is thicker compared to the channel width. However, because the values calculated for *Pe* previously are low, diffusion is still expected to combat concentration gradients. Other factors explored in the context of planarization during spin coating include polymer molecular weight and solvent[69], feature width/depth[66,70], and ink concentration/volume[71].

Solutal Marangoni flows must also be considered during the planarization process. The appearance of a surface concentration gradient during drying could induce an additional surface-tension gradient that drives Marangoni flow. However, measurements of the effect of solute concentration on surface tension (see supporting information Fig. S5) suggest that the concentration of P3HT has a minor effect on the surface tension of the solution, with a change of

< 1 mN/m. Thus, the effects of solutal Marangoni flow on planarization are expected to be minor in the P3HT/oDCB system.

Given the similarity between the drying on the mesa and planarization over the channels, it appears that in both cases of a drying droplet pinned on a flat surface and a drying film over a recessed channel, lower drying temperatures result in more time for lateral diffusion, leading to improved uniformity. In the former, the nonuniform evaporation that leads to the coffee-ring effect is mitigated by slower drying. When drying is slower, the resultant *Pe* is smaller, indicating the increased influence of diffusion relative to advection. In the latter, slower drying results in a slower descent of the evaporating free surface. Due to the nonuniform substrate topography, concentration gradients form that—when given more time (as in the case of lower drying temperatures)—enable lateral diffusion of solute to fill in the underlying recessed channel. The relative effects of evaporation and diffusion are again at play and are described using the same *Pe*. In both frameworks, reducing the drying temperature enhances lateral diffusion relative to evaporation and improves the uniformity of the final film upon complete drying.

3.4 Diode Performance

The techniques used to achieve increased uniformity and planarization were applied in the processing of SCALE mesa diodes. Figure 7 summarizes the electrical performance and device-cross sections of completed Schottky diodes using the mesa design with the P3HT dried at 23°C. The cross-section taken at the channel (Fig. 7a) demonstrates the successful application of planarization to achieve filled-in P3HT channels and a planar surface despite a nonuniform underlying topography. The planar P3HT deposition prevents unwanted contact between the top PEDOT:PSS and bottom Ag layers that have limited previous SCALE diodes.[13] The cross-section at the center of the mesa (Fig. 7b) demonstrates the deposition of a sub-300 nm thin layer of P3HT

in the diode. The individual layers are distinguishable and the top PEDOT:PSS layer does not contact the underlying Ag layer. Prior to cross-sectioning, the diodes were embedded in epoxy to facilitate sectioning.

The current-voltage (I-V) curves (Fig. 7c) of the mesa diodes were obtained by sweeping voltage from -1 to 1 V at a rate of 0.2 V/s to the PEDOT:PSS top contact while grounding the Ag bottom contact and measuring the current, as shown in the inset. I-V curves are shown on both a linear and semilogarithmic scale to demonstrate the rectification capabilities of the diode. To assess the diode reproducibility, the statistical characteristics of 25 fabricated devices are shown in Figure 7d. Each data point in the I-V curve represents the average value across all devices, while the shaded regions indicate the standard deviation. The inset displays a histogram for the distribution of the log(rectification ratio), where the rectification ratio is defined as the ratio between the on/off current at ±1 V.

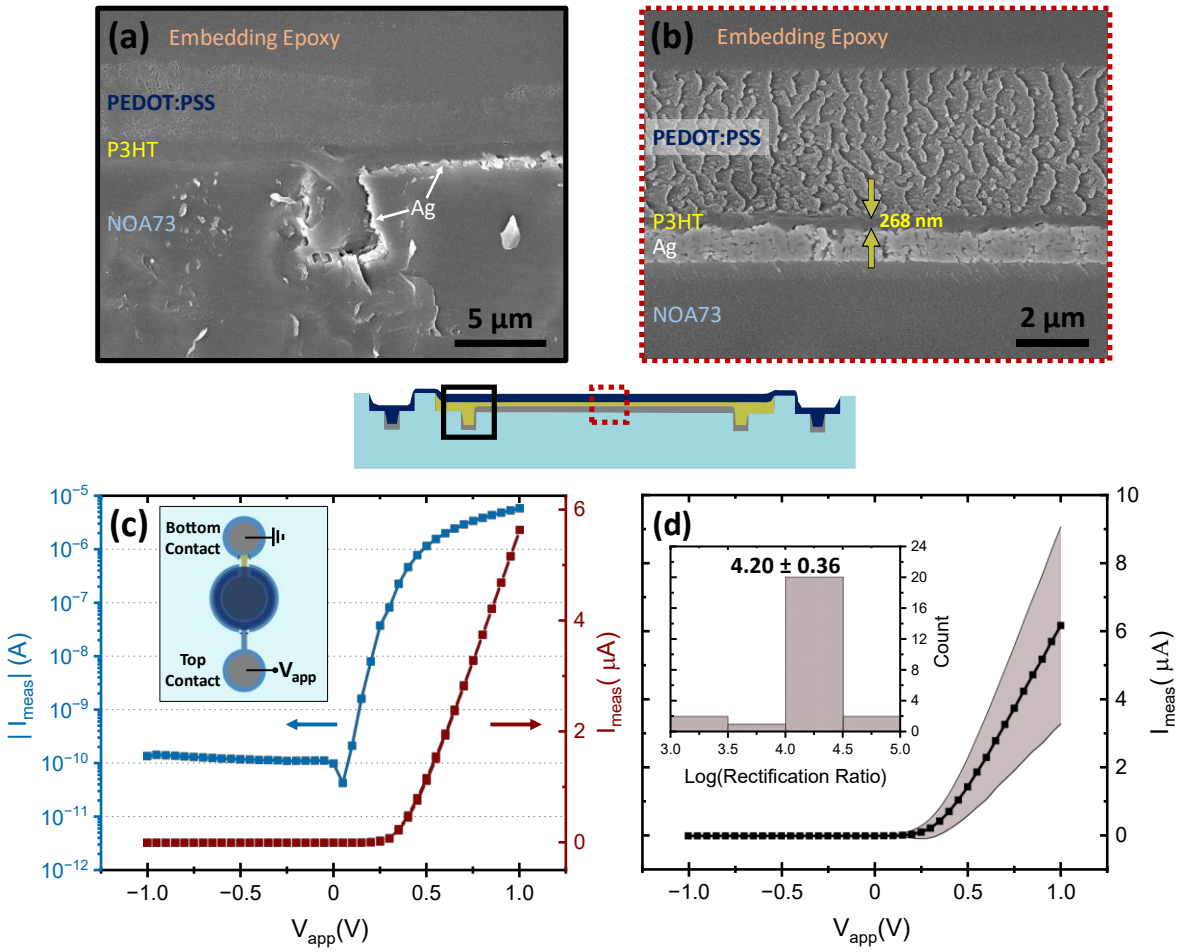

Figure 7. Characterization of SCALE mesa diodes. Cross-sectional scanning electron micrographs show the device stack taken at the (a) left channel and (b) mesa center. The schematic indicates the location of each micrograph relative to the overall diode structure. The electronic performance for a single diode is plotted as (c) applied voltage versus measured current using both a linear (red, right) and semi-log (blue, left) scale. The inset depicts the electrical measurement setup. (d) Shows the statistical characteristics of 25 fabricated diodes. Data points represent the arithmetic mean taken over all devices, while shaded regions represent ±standard deviation. The inset displays a histogram of the log(rectification ratio) distribution across the devices along with the average and standard deviation.

By utilizing the processing insights obtained from the mesa uniformity and planarization studies discussed earlier, the performance of the SCALE mesa diodes has surpassed that of previous SCALE diodes.[13] The Schottky diodes in this study have P3HT thicknesses in the sub-300 nm regime, which is thinner than those achieved in other printed diodes.[13,42,72,73] Thin P3HT layers are

advantageous because they decrease the bulk resistance in series with the rectifying Ag-P3HT interface. Furthermore, drying the P3HT solution layer at lower temperatures was found to also improve the device yield. Here, yield is defined as the number of printed devices that exhibit rectification ratios $\geq 10^3$ out of the total number of devices. Drying the deposited P3HT solution at 120°C resulted in a yield of only 9% (3/33 devices). However, when the P3HT solution layer was dried at 23°C, a yield of 69% (25/36 devices) was achieved, indicating a nearly 8x improvement in yield solely by changing the drying temperature. This improvement is attributed to the successful planarization of the channels around the mesa at lower drying temperatures, reducing the occurrence of short-circuit failures. Furthermore, in prior SCALE work, the yield dropped to 22% when using 500 nm thin P3HT.[13] Here, a 69% yield was maintained even at 300 nm thin P3HT layers, confirming the capability of the mesa diode design to successfully mitigate short-circuits.

SCALE Schottky diodes using the mesa design also demonstrate excellent rectification capabilities, as shown in Figure 7c. The diodes exhibit minimal hysteresis and a low turn-on voltage of ~0.3 V. Rectification ratios as high as 4.0×10^4 at ±1 V were achieved. These results are comparable to or better than other diodes demonstrated in the literature.[6,13,74–76] Higher rectification ratios up to 10^6 have been reported for printed organic diodes by using higher mobility semiconductors.[42] However, the processing principles described in the current study can be translated and applied towards other solution-processed materials systems. Figure 7d also demonstrates the reproducibility of the SCALE mesa diodes. Across all 25 diodes, the on-current has a ±2.89 μA deviation at 1 V and the off-current has a deviation of only ±1.93 nA at -1 V. As seen in the inset of Figure 7d, the diodes had an average rectification ratio of $10^{4.2\pm0.36}$, with 20/25 of the diodes having rectification ratios between 10^4 and $10^{4.5}$, emphasizing the device

reproducibility. Achieving low device variability is especially important in R2R processes in which thousands of devices are produced. Reproducibility is also critical when combining discrete devices into a circuit because individual device variability can cascade into variability of the overall circuit performance (e.g., a full-wave rectifier circuit using four diodes). The diodes demonstrated herein also have a relatively small device active area of ~0.16 mm^2, which is smaller than other diodes typically fabricated using printing techniques.[6,42,72,76] The small device area is connected to the high resolution and layer-on-layer registration made possible via the combination of microimprinting and inkjet printing in the SCALE process.

4. Conclusion

The present study demonstrates the effects and importance of controlling processing parameters like drying temperature for fabricating solution-processed electronic devices. Printed organic Schottky diodes were created using SCALE, a process that utilizes capillary flow to pattern electronic inks into a network of reservoirs and channels. We developed a new design for diodes that incorporates a mesa structure to mitigate failure caused by shorting between the top and bottom contacts. For the P3HT solutions used to create the semiconductor layer in the diode, reduced drying temperatures were shown to mitigate the coffee-ring effect in pinned drying droplets. The same principles seen in the case of a pinned droplet were shown to also apply to the planarization of films deposited over topographic features. The effects of drying temperature on both uniformity and planarization were encapsulated using a Péclet number that quantifies the competition between evaporation and diffusion. We demonstrate that through this approach, film uniformity for both situations can be described using a single *Pe*.

By applying the demonstrated processing principles, functional Schottky diodes using the mesa design reproducibly exhibited high rectification ratio (10^4) and thin (<300 nm) active layers across

a 0.16 mm^2 active region areal footprint. The fabricated diodes utilized all additive techniques while maintaining compatibility with R2R processing. In future work, the discrete diodes demonstrated here can be integrated into full electronic circuits (e.g., rectifiers, RFID tags, sensors). Furthermore, findings on uniformity and planarization translate well into thin-film transistors and capacitors, in which careful control of thickness is strongly correlated with device performance. Thus, this work provides a foundational basis for improving a spectrum of solution-processed electronic devices.

Associated Content

Supporting Information. Additional details on the silicon wafer template pattern fabrication method; dimensions of the mesa diode design; optical micrographs of each layer in a device; contact angle measurement; surface tension measurement; estimations of Peclet number for both the mesa uniformity and planarization studies. (Section/Figures S1-S10) (PDF)

Author information

Corresponding Authors

*Email: frisbie@umn.edu

*Email: lfrancis@umn.edu

ORCID

Jonathan D. Nguyen: 0009-0003-5683-731X

Satish Kumar: 0000-0003-0829-6355

C. Daniel Frisbie: 0000-0002-4735-2228

Lorraine F. Francis: 0000-0003-2516-2957

Author Contributions

The manuscript was written through contributions of all authors. All authors have given approval to the final version of the manuscript.

Acknowledgements

This work was supported by the National Science Foundation (NSF) under grant number CMMI 2038722. The authors thank Nate Hartnett, Li-Hsuan Chang, Matthew Hausladen, Chinmayee Panigrahi, and Prof. Christopher Ellison for valuable discussions. Special thanks to Dr. Krystopher Jochem for training, mentorship, and the initial conceptualization of the mesa diode design. Portions of this work were conducted in the Minnesota Nano Center, which is supported by the National Science Foundation through the National Nanotechnology Coordinated Infrastructure (NNCI) under Award Number ECCS-2025124. Parts of this work were carried out in the Characterization Facility at the University of Minnesota, which receives partial support from the NSF through the MRSEC (Award Number DMR-2011401) and the NNCI (Award Number ECCS-2025124) programs.

References

(1) Lo, L.-W.; Shi, H.; Wan, H.; Xu, Z.; Tan, X.; Wang, C. Inkjet-Printed Soft Resistive Pressure Sensor Patch for Wearable Electronics Applications. *Adv. Mater. Technol.* **2020**, *5* (1), 1900717. https://doi.org/10.1002/admt.201900717.

(2) Quintero, A. V.; Molina-Lopez, F.; Smits, E. C. P.; Danesh, E.; Brand, J. van den; Persaud, K.; Oprea, A.; Barsan, N.; Weimar, U.; Rooij, N. F. de; Briand, D. Smart RFID Label with a Printed Multisensor Platform for Environmental Monitoring. *Flex. Print. Electron.* **2016**, *1* (2), 025003. https://doi.org/10.1088/2058-8585/1/2/025003.

(3) Al Shboul, A. M.; Izquierdo, R. Printed Chemiresistive In2O3 Nanoparticle-Based Sensors with Ppb Detection of H2S Gas for Food Packaging. *ACS Appl. Nano Mater.* **2021**, *4* (9), 9508–9517. https://doi.org/10.1021/acsanm.1c01970.

(4) Bonnassieux, Y.; Brabec, C. J.; Cao, Y.; Carmichael, T. B.; Chabinyc, M. L.; Cheng, K.-T.; Cho, G.; Chung, A.; Cobb, C. L.; Distler, A.; Egelhaaf, H.-J.; Grau, G.; Guo, X.; Haghiashtiani, G.; Huang, T.-C.; Hussain, M. M.; Iniguez, B.; Lee, T.-M.; Li, L.; Ma, Y.; Ma, D.; McAlpine, M. C.; Ng, T. N.; Österbacka, R.; Patel, S. N.; Peng, J.; Peng, H.; Rivnay, J.; Shao, L.; Steingart, D.; Street, R. A.; Subramanian, V.; Torsi, L.; Wu, Y. The 2021 Flexible and Printed Electronics Roadmap. *Flex. Print. Electron.* **2021**, *6* (2), 023001. https://doi.org/10.1088/2058-8585/abf986.

(5) Kim, Y. Y.; Yang, T.-Y.; Suhonen, R.; Kemppainen, A.; Hwang, K.; Jeon, N. J.; Seo, J. Roll-to-Roll Gravure-Printed Flexible Perovskite Solar Cells Using Eco-Friendly Antisolvent Bathing with Wide Processing Window. *Nat. Commun.* **2020**, *11* (1), 5146. https://doi.org/10.1038/s41467-020-18940-5.

(6) Lilja, K. E.; Bäcklund, T. G.; Lupo, D.; Hassinen, T.; Joutsenoja, T. Gravure Printed Organic Rectifying Diodes Operating at High Frequencies. *Org. Electron.* **2009**, *10* (5), 1011–1014. https://doi.org/10.1016/j.orgel.2009.04.008.

(7) Ryu, G. S.; Kim, J. S.; Jeong, S. H.; Song, C. K. A Printed OTFT-Backplane for AMOLED Display. *Org. Electron.* **2013**, *14* (4), 1218–1224. https://doi.org/10.1016/j.orgel.2013.02.006.

(8) Mattana, G.; Loi, A.; Woytasik, M.; Barbaro, M.; Noël, V.; Piro, B. Inkjet-Printing: A New Fabrication Technology for Organic Transistors. *Adv. Mater. Technol.* **2017**, *2* (10), 1700063. https://doi.org/10.1002/admt.201700063.

(9) Gao, M.; Li, L.; Song, Y. Inkjet Printing Wearable Electronic Devices. *J. Mater. Chem. C* **2017**, *5* (12), 2971–2993. https://doi.org/10.1039/C7TC00038C.

(10) da Costa, T. H.; Choi, J.-W. Low-Cost and Customizable Inkjet Printing for Microelectrodes Fabrication. *Micro Nano Syst. Lett.* **2020**, *8* (1), 2. https://doi.org/10.1186/s40486-020-0104-7.

(11) Cao, M.; Jochem, K.; Hyun, W. J.; Francis, L. F.; Frisbie, C. D. Self-Aligned Inkjet Printing of Resistors and Low-Pass Resistor–Capacitor Filters on Roll-to-Roll Imprinted Plastics with Resistances Ranging from 10 to 10 6 ${upOmega. *Flex. Print. Electron.* **2018**, *3* (4), 045003. https://doi.org/10.1088/2058-8585/aaeb6c.

(12) Hyun, W. J.; Secor, E. B.; Kim, C.-H.; Hersam, M. C.; Francis, L. F.; Frisbie, C. D. Scalable, Self-Aligned Printing of Flexible Graphene Micro-Supercapacitors. *Adv. Energy Mater.* **2017**, *7* (17), 1700285. https://doi.org/10.1002/aenm.201700285.

(13) Cao, M.; Hyun, W. J.; Francis, L. F.; Frisbie, C. D. Inkjet-Printed, Self-Aligned Organic Schottky Diodes on Imprinted Plastic Substrates. *Flex. Print. Electron.* **2020**, *5* (1), 015006. https://doi.org/10.1088/2058-8585/ab670a.

(14) Jochem, K. S.; Suszynski, W. J.; Frisbie, C. D.; Francis, L. F. High-Resolution, High-Aspect-Ratio Printed and Plated Metal Conductors Utilizing Roll-to-Roll Microscale UV Imprinting with Prototype Imprinting Stamps. *Ind. Eng. Chem. Res.* **2018**, *57* (48), 16335–16346. https://doi.org/10.1021/acs.iecr.8b03619.

(15) Jochem, K. S.; Kolliopoulos, P.; Frisbie, C. D.; Francis, L. F. Solution-Based, Additive Fabrication of Flush Metal Conductors in Plastic Substrates by Printing and Plating in Two-Level Capillary Channels. *Flex. Print. Electron.* **2021**, *6* (4), 045005. https://doi.org/10.1088/2058-8585/ac298a.

(16) Hyun, W. J.; Secor, E. B.; Bidoky, F. Z.; Walker, S. B.; Lewis, J. A.; Hersam, M. C.; Francis, L. F.; Frisbie, C. D. Self-Aligned Capillarity-Assisted Printing of Top-Gate Thin-Film Transistors on Plastic. *Flex. Print. Electron.* **2018**, *3* (3), 035004. https://doi.org/10.1088/2058-8585/aad476.

(17) Song, D.; Zare Bidoky, F.; Hyun, W. J.; Walker, S. B.; Lewis, J. A.; Frisbie, C. D. All-Printed, Self-Aligned Carbon Nanotube Thin-Film Transistors on Imprinted Plastic Substrates. *ACS Appl. Mater. Interfaces* **2018**, *10* (18), 15926–15932. https://doi.org/10.1021/acsami.8b01581.

(18) Jochem, K. S.; Kolliopoulos, P.; Zare Bidoky, F.; Wang, Y.; Kumar, S.; Frisbie, C. D.; Francis, L. F. Self-Aligned Capillarity-Assisted Printing of High Aspect Ratio Flexible Metal Conductors: Optimizing Ink Flow, Plating, and Mechanical Adhesion. *Ind. Eng. Chem. Res.* **2020**, *59* (51), 22107–22122. https://doi.org/10.1021/acs.iecr.0c03081.

(19) Deegan, R. D.; Bakajin, O.; Dupont, T. F.; Huber, G.; Nagel, S. R.; Witten, T. A. Capillary Flow as the Cause of Ring Stains from Dried Liquid Drops. *Nature* **1997**, *389* (6653), 827–829. https://doi.org/10.1038/39827.

(20) Deegan, R. D.; Bakajin, O.; Dupont, T. F.; Huber, G.; Nagel, S. R.; Witten, T. A. Contact Line Deposits in an Evaporating Drop. *Phys. Rev. E* **2000**, *62* (1), 756–765. https://doi.org/10.1103/PhysRevE.62.756.

(21) Routh, A. F. Drying of Thin Colloidal Films. *Rep. Prog. Phys.* **2013**, *76* (4), 046603. https://doi.org/10.1088/0034-4885/76/4/046603.

(22) Mampallil, D. Some Physics inside Drying Droplets. *Resonance* **2014**, *19* (2), 123–134. https://doi.org/10.1007/s12045-014-0016-z.

(23) Hu, H.; Larson, R. G. Evaporation of a Sessile Droplet on a Substrate. *J. Phys. Chem. B* **2002**, *106* (6), 1334–1344. https://doi.org/10.1021/jp0118322.

(24) Hu, H.; Larson, R. G. Analysis of the Microfluid Flow in an Evaporating Sessile Droplet. *Langmuir* **2005**, *21* (9), 3963–3971. https://doi.org/10.1021/la047528s.

(25) Al-Milaji, K. N.; Zhao, H. New Perspective of Mitigating the Coffee-Ring Effect: Interfacial Assembly. *J. Phys. Chem. C* **2019**, *123* (19), 12029–12041. https://doi.org/10.1021/acs.jpcc.9b00797.

(26) Pham, T.; Kumar, S. Drying of Droplets of Colloidal Suspensions on Rough Substrates. *Langmuir* **2017**, *33* (38), 10061–10076. https://doi.org/10.1021/acs.langmuir.7b02341.

(27) Hu, H.; Larson, R. G. Marangoni Effect Reverses Coffee-Ring Depositions. *J. Phys. Chem. B* **2006**, *110* (14), 7090–7094. https://doi.org/10.1021/jp0609232.

(28) Seo, C.; Jang, D.; Chae, J.; Shin, S. Altering the Coffee-Ring Effect by Adding a Surfactant-like Viscous Polymer Solution. *Sci. Rep.* **2017**, *7* (1), 500. https://doi.org/10.1038/s41598-017-00497-x.

(29) Kim, H.; Boulogne, F.; Um, E.; Jacobi, I.; Button, E.; Stone, H. A. Controlled Uniform Coating from the Interplay of Marangoni Flows and Surface-Adsorbed Macromolecules. *Phys. Rev. Lett.* **2016**, *116* (12), 124501. https://doi.org/10.1103/PhysRevLett.116.124501.

(30) Dugyala, V. R.; Basavaraj, M. G. Control over Coffee-Ring Formation in Evaporating Liquid Drops Containing Ellipsoids. *Langmuir* **2014**, *30* (29), 8680–8686. https://doi.org/10.1021/la500803h.

(31) Bhardwaj, R.; Fang, X.; Somasundaran, P.; Attinger, D. Self-Assembly of Colloidal Particles from Evaporating Droplets: Role of DLVO Interactions and Proposition of a Phase Diagram. *Langmuir* **2010**, *26* (11), 7833–7842. https://doi.org/10.1021/la9047227.

(32) Kajiya, T.; Doi, M. Dynamics of Drying Process of Polymer Solution Droplets: Analysis of Polymer Transport and Control of Film Profiles. *Nihon Reoroji Gakkaishi* **2011**, *39* (1_2), 17–28. https://doi.org/10.1678/rheology.39.17.

(33) Kajiya, T.; Kobayashi, W.; Okuzono, T.; Doi, M. Controlling the Drying and Film Formation Processes of Polymer Solution Droplets with Addition of Small Amount of Surfactants. *J. Phys. Chem. B* **2009**, *113* (47), 15460–15466. https://doi.org/10.1021/jp9077757.

(34) Jung, Y.; Kajiya, T.; Yamaue, T.; Doi, M. Film Formation Kinetics in the Drying Process of Polymer Solution Enclosed by Bank. *Jpn. J. Appl. Phys.* **2009**, *48* (3R), 031502. https://doi.org/10.1143/JJAP.48.031502.

(35) Eales, A. D.; Routh, A. F.; Dartnell, N.; Simon, G. Evaporation of Pinned Droplets Containing Polymer – an Examination of the Important Groups Controlling Final Shape. *AIChE J.* **2015**, *61* (5), 1759–1767. https://doi.org/10.1002/aic.14777.

(36) Kraft, T. M.; Berger, P. R.; Lupo, D. Printed and Organic Diodes: Devices, Circuits and Applications. *Flex. Print. Electron.* **2017**, *2* (3), 033001. https://doi.org/10.1088/2058-8585/aa8ac3.

(37) Loganathan, K.; Scaccabarozzi, A. D.; Faber, H.; Ferrari, F.; Bizak, Z.; Yengel, E.; Naphade, D. R.; Gedda, M.; He, Q.; Solomeshch, O.; Adilbekova, B.; Yarali, E.; Tsetseris, L.; Salama, K. N.; Heeney, M.; Tessler, N.; Anthopoulos, T. D. 14 GHz Schottky Diodes Using a P-Doped Organic Polymer. *Adv. Mater.* **2022**, *34* (22), 2108524. https://doi.org/10.1002/adma.202108524.

(38) Chaudhary, V.; Kumar, N.; Singh, A. K. Solubility Dependent Trap Density in Poly (3-Hexylthiophene) Organic Schottky Diodes at Room Temperature. *Synth. Met.* **2019**, *250*, 88–93. https://doi.org/10.1016/j.synthmet.2019.03.006.

(39) Şahin, B.; Çetin, H.; Ayyildiz, E. The Effect of Series Resistance on Capacitance–Voltage Characteristics of Schottky Barrier Diodes. *Solid State Commun.* **2005**, *135* (8), 490–495. https://doi.org/10.1016/j.ssc.2005.05.050.

(40) Cibils, R. M.; Buitrago, R. H. Forward *I - V* Plot for Nonideal Schottky Diodes with High Series Resistance. *J. Appl. Phys.* **1985**, *58* (2), 1075–1077. https://doi.org/10.1063/1.336222.

(41) Chu, Y.; Qian, C.; Chahal, P.; Cao, C. Printed Diodes: Materials Processing, Fabrication, and Applications. *Adv. Sci.* **2019**, *6* (6), 1801653. https://doi.org/10.1002/advs.201801653.

(42) Viola, F. A.; Brigante, B.; Colpani, P.; Dell'Erba, G.; Mattoli, V.; Natali, D.; Caironi, M. A 13.56 MHz Rectifier Based on Fully Inkjet Printed Organic Diodes. *Adv. Mater.* **2020**, *32* (33), 2002329. https://doi.org/10.1002/adma.202002329.

(43) Savenije, T. J.; Kroeze, J. E.; Yang, X.; Loos, J. The Formation of Crystalline P3HT Fibrils upon Annealing of a PCBM:P3HT Bulk Heterojunction. *Thin Solid Films* **2006**, *511–512*, 2–6. https://doi.org/10.1016/j.tsf.2005.12.123.

(44) Huang, Y.-C.; Liao, Y.-C.; Li, S.-S.; Wu, M.-C.; Chen, C.-W.; Su, W.-F. Study of the Effect of Annealing Process on the Performance of P3HT/PCBM Photovoltaic Devices Using Scanning-Probe Microscopy. *Sol. Energy Mater. Sol. Cells* **2009**, *93* (6), 888–892. https://doi.org/10.1016/j.solmat.2008.10.027.

(45) Shi, H.; Liu, C.; Jiang, Q.; Xu, J. Effective Approaches to Improve the Electrical Conductivity of PEDOT:PSS: A Review. *Adv. Electron. Mater.* **2015**, *1* (4), 1500017. https://doi.org/10.1002/aelm.201500017.

(46) Murakami, T.; Mori, Y.; Okuzaki, H. Effect of Ethylene Glycol on Structure and Carrier Transport in Highly Conductive Poly(3,4-Ethylenedioxythiophene)/Poly(4-Styrenesulfonate). *Trans. Mater. Res. Soc. Jpn.* **2011**, *36* (2), 165–168. https://doi.org/10.14723/tmrsj.36.165.

(47) Tevi, T.; Saint Birch, S. W.; Thomas, S. W.; Takshi, A. Effect of Triton X-100 on the Double Layer Capacitance and Conductivity of Poly(3,4-Ethylenedioxythiophene):Poly(Styrenesulfonate) (PEDOT:PSS) Films. *Synth. Met.* **2014**, *191*, 59–65. https://doi.org/10.1016/j.synthmet.2014.02.005.

(48) Zhou, X.; Dong, X.; Liu, Y.; Wang, W.; Wei, W.; Chen, J.; Liu, T.; Zhou, Y. Effect of Wetting Surfactants on the Work Function of PEDOT:PSS for Organic Solar Cells. *ACS Appl. Energy Mater.* **2022**, *5* (3), 3766–3772. https://doi.org/10.1021/acsaem.2c00217.

(49) Huang, J.; Miller, P. F.; Wilson, J. S.; de Mello, A. J.; de Mello, J. C.; Bradley, D. D. C. Investigation of the Effects of Doping and Post-Deposition Treatments on the Conductivity, Morphology, and Work Function of Poly(3,4-Ethylenedioxythiophene)/Poly(Styrene Sulfonate) Films. *Adv. Funct. Mater.* **2005**, *15* (2), 290–296. https://doi.org/10.1002/adfm.200400073.

(50) Sowade, E.; Kang, H.; Y. Mitra, K.; J. Weiß, O.; Weber, J.; R. Baumann, R. Roll-to-Roll Infrared (IR) Drying and Sintering of an Inkjet-Printed Silver Nanoparticle Ink within 1 Second. *J. Mater. Chem. C* **2015**, *3* (45), 11815–11826. https://doi.org/10.1039/C5TC02291F.

(51) Jung, S.; Yun Choi, D.; Moon Lee, H. Roll-to-Roll Processed, Highly Conductive, and Flexible Aluminum (Al) Electrodes Based on Al Precursor Inks. *RSC Adv.* **2018**, *8* (36), 19950–19957. https://doi.org/10.1039/C8RA03303J.

(52) Kim, J.-H.; Park, S.-B.; Kim, J. H.; Zin, W.-C. Polymer Transports Inside Evaporating Water Droplets at Various Substrate Temperatures. *J. Phys. Chem. C* **2011**, *115* (31), 15375–15383. https://doi.org/10.1021/jp202429p.

(53) Baskaran, R.; Kubendran, T. R. Thermophysical Properties of *Para* -Anisaldehyde (1) + Chlorobenzene (2) at Temperatures of (303.15, 313.15, and 323.15) K and a Pressure of 0.1 MPa. *J. Chem. Eng. Data* **2008**, *53* (4), 978–982. https://doi.org/10.1021/je700714m.

(54) Poser, C. I.; Sanchez, I. C. Surface Tension Theory of Pure Liquids and Polymer Melts. *J. Colloid Interface Sci.* **1979**, *69* (3), 539–548. https://doi.org/10.1016/0021-9797(79)90142-5.

(55) Ristenpart, W. D.; Kim, P. G.; Domingues, C.; Wan, J.; Stone, H. A. Influence of Substrate Conductivity on Circulation Reversal in Evaporating Drops. *Phys. Rev. Lett.* **2007**, *99* (23), 234502. https://doi.org/10.1103/PhysRevLett.99.234502.

(56) Yaws, C. L. Chapter 7 - Thermal Conductivity of Liquid – Organic Compounds. In *Transport Properties of Chemicals and Hydrocarbons*; Yaws, C. L., Ed.; William Andrew Publishing: Boston, 2009; pp 299–395. https://doi.org/10.1016/B978-0-8155-2039-9.50012-0.

(57) Fujigaya, T.; Fukumaru, T.; Nakashima, N. Evaluation of Dispersion State and Thermal Conductivity Measurement of Carbon Nanotubes/UV-Curable Resin Nanocomposites. *Synth. Met.* **2009**, *159* (9), 827–830. https://doi.org/10.1016/j.synthmet.2009.01.019.

(58) Lee, S.; Kim, Y.; Park, D.; Kim, J. The Thermal Properties of a UV Curable Acrylate Composite Prepared by Digital Light Processing 3D Printing. *Compos. Commun.* **2021**, *26*, 100796. https://doi.org/10.1016/j.coco.2021.100796.

(59) Pham, T.; Cheng, X.; Kumar, S. Drying of Multicomponent Thin Films on Substrates with Topography. *J. Polym. Sci. Part B Polym. Phys.* **2017**, *55* (22), 1681–1691. https://doi.org/10.1002/polb.24276.

(60) Jarusuwannapoom, T.; Hongrojjanawiwat, W.; Jitjaicham, S.; Wannatong, L.; Nithitanakul, M.; Pattamaprom, C.; Koombhongse, P.; Rangkupan, R.; Supaphol, P. Effect of Solvents on Electro-Spinnability of Polystyrene Solutions and Morphological Appearance of Resulting Electrospun Polystyrene Fibers. *Eur. Polym. J.* **2005**, *41* (3), 409–421. https://doi.org/10.1016/j.eurpolymj.2004.10.010.

(61) Roché, M.; Li, Z.; Griffiths, I. M.; Le Roux, S.; Cantat, I.; Saint-Jalmes, A.; Stone, H. A. Marangoni Flow of Soluble Amphiphiles. *Phys. Rev. Lett.* **2014**, *112* (20), 208302. https://doi.org/10.1103/PhysRevLett.112.208302.

(62) Gommes, C. J.; Tharakan, J. The Péclet Number of a Casino: Diffusion and Convection in a Gambling Context. *Am. J. Phys.* **2020**, *88* (6), 439–447. https://doi.org/10.1119/10.0000957.

(63) Rubinstein, M.; Colby, R. H. *Polymer Physics*; Oxford University Press, 2003.

(64) Hiemenz, P. C.; Lodge, T. P. *Polymer Chemistry*, 2nd ed.; CRC Press: Boca Raton, 2007. https://doi.org/10.1201/9781420018271.

(65) Okuzono, T.; Kobayashi, M.; Doi, M. Final Shape of a Drying Thin Film. *Phys. Rev. E* **2009**, *80* (2), 021603. https://doi.org/10.1103/PhysRevE.80.021603.

(66) Bornside, D. E. Mechanism for the Local Planarization of Microscopically Rough Surfaces by Drying Thin Films of Spin-Coated Polymer/Solvent Solutions. *J. Electrochem. Soc.* **1990**, *137* (8), 2589. https://doi.org/10.1149/1.2086992.

(67) Stillwagon, L. E.; Larson, R. G.; Taylor, G. N. Planarization of Substrate Topography by Spin Coating. *J. Electrochem. Soc.* **1987**, *134* (8), 2030–2037. https://doi.org/10.1149/1.2100813.

(68) Stillwagon, L. E.; Larson, R. G. Leveling of Thin Films over Uneven Substrates during Spin Coating. *Phys. Fluids Fluid Dyn.* **1990**, *2* (11), 1937–1944. https://doi.org/10.1063/1.857669.

(69) Bullwinkel, M. D.; Gu, J.; Campbell, G. A.; Sukanek, P. C. The Effect of Polymer Molecular Weight and Solvent Type on the Planarization of Spin-Coated Films. *J. Electrochem. Soc.* **1995**, *142* (7), 2389. https://doi.org/10.1149/1.2044307.

(70) Schiltz, A. An Empirical Model for Planarization with Polymer Solutions. *Jpn. J. Appl. Phys.* **1995**, *34* (Part 1, No. 8A), 4185–4194. https://doi.org/10.1143/JJAP.34.4185.

(71) LaVergne, D.; Hofer, D. Modeling Planarization With Polymers. *Proc. SPIE* **1985**. https://doi.org/10.1117/12.947823.

(72) Heljo, P. S.; Li, M.; Lilja, K. E.; Majumdar, H. S.; Lupo, D. Printed Half-Wave and Full-Wave Rectifier Circuits Based on Organic Diodes. *IEEE Trans. Electron Devices* **2013**, *60* (2), 870–874. https://doi.org/10.1109/TED.2012.2233741.

(73) Lilja, K. E.; Majumdar, H. S.; Pettersson, F. S.; Österbacka, R.; Joutsenoja, T. Enhanced Performance of Printed Organic Diodes Using a Thin Interfacial Barrier Layer. *ACS Appl. Mater. Interfaces* **2011**, *3* (1), 7–10. https://doi.org/10.1021/am1009869.

(74) Conti, S.; Martínez-Domingo, C.; Lay, M.; Terés, L.; Vilaseca, F.; Ramon, E. Nanopaper-Based Organic Inkjet-Printed Diodes. *Adv. Mater. Technol.* **2020**, *5* (6), 1900773. https://doi.org/10.1002/admt.201900773.

(75) Lin, C.-Y.; Tsai, C.-H.; Lin, H.-T.; Chang, L.-C.; Yeh, Y.-H.; Pei, Z.; Peng, Y.-R.; Wu, C.-C. High-Frequency Polymer Diode Rectifiers for Flexible Wireless Power-Transmission Sheets. *Org. Electron.* **2011**, *12* (11), 1777–1782. https://doi.org/10.1016/j.orgel.2011.07.006.

(76) Ng, T. N.; Schwartz, D. E.; Mei, P.; Kor, S.; Veres, J.; Bröms, P.; Karlsson, C. Pulsed Voltage Multiplier Based on Printed Organic Devices. *Flex. Print. Electron.* **2015**, *1* (1), 015002. https://doi.org/10.1088/2058-8585/1/1/015002.

For Table of Contents Only